nature photonics

Article

https://doi.org/10.1038/s41566-023-01257-2

Soliton pulse pairs at multiple colours in normal dispersion microresonators

In the format provided by the authors and unedited

I. EIGENMODES OF A TWO-RING COUPLED RESONATOR

In this section we study the coupling between the two coupled rings and analyze the mode frequencies of the compound system. Eigenfrequencies of coupled resonators have traditionally been calculated from a coupled-mode perspective, where modal coupling are calculated as off-diagonal matrix elements. However, this approach becomes unfeasible in the current system as one longitudinal mode will couple to infinitely many modes from the opposite ring because mode number matching is not required. The dependence of coupling with respect to wavelength is also difficult to implement. To circumvent these problems, we instead use a transfer function formalism to determine the mode frequencies.

The resonator schematic is shown in Fig. S1. L_A and L_B are the circumferences of the right and left ring, respectively, L_co is the length of the coupling region, c is the speed of light in vacuum, and $n_\mathrm{wg}(\omega)$ is the effective phase index of the fundamental mode in the SiN waveguide at optical angular frequency ω. By defining a single index along the waveguide, we have neglected the geometric dispersions resulting from bending the waveguide. These have been shown to be small compared to the geometric dispersion induced by waveguide confinement. We now assume that light with a single frequency is propagating in the system. At the points opposite to the coupling region, the field amplitude in each ring is denoted as $\psi_\mathrm{I,A}$ and $\psi_\mathrm{I,B}$. These amplitudes can be assembled into a vector as $\psi_\mathrm{I} = (\psi_\mathrm{I,A}, \psi_\mathrm{I,B})^\mathbf{T}$, where $^\mathbf{T}$ denotes the transpose of a vector or matrix. Similarly, the field just before the coupling part can be found as

$$\begin{pmatrix}\psi_\mathrm{II,A}\\ \psi_\mathrm{II,B}\end{pmatrix} = \begin{pmatrix}e^{in_\mathrm{wg}\omega(L_\mathrm{A}-L_\mathrm{co})/(2c)} & 0\\ 0 & e^{in_\mathrm{wg}\omega(L_\mathrm{B}-L_\mathrm{co})/(2c)}\end{pmatrix}\begin{pmatrix}\psi_\mathrm{I,A}\\ \psi_\mathrm{I,B}\end{pmatrix} \tag{S1}$$

For the coupling section, we denote the coupling rate per unit length as g_co. The coupling depends on ω, and is assumed to be uniform along the coupling section (i.e., boundary effects from adiabatic bends are included in the effective coupling length). The field after the coupling section can be expressed with a matrix exponential:

$$\begin{pmatrix}\psi_\mathrm{III,A}\\ \psi_\mathrm{III,B}\end{pmatrix} = \exp\left[iL_\mathrm{co}\begin{pmatrix}n_\mathrm{wg}\omega/c & g_\mathrm{co}\\ g_\mathrm{co} & n_\mathrm{wg}\omega/c\end{pmatrix}\right]\begin{pmatrix}\psi_\mathrm{II,A}\\ \psi_\mathrm{II,B}\end{pmatrix} \tag{S2}$$

Finally, returning to the points opposite to the coupling region, the field reads

$$\begin{pmatrix}\psi_\mathrm{IV,A}\\ \psi_\mathrm{IV,B}\end{pmatrix} = \begin{pmatrix}e^{in_\mathrm{wg}\omega(L_\mathrm{A}-L_\mathrm{co})/(2c)} & 0\\ 0 & e^{in_\mathrm{wg}\omega(L_\mathrm{B}-L_\mathrm{co})/(2c)}\end{pmatrix}\begin{pmatrix}\psi_\mathrm{III,A}\\ \psi_\mathrm{III,B}\end{pmatrix} \tag{S3}$$

For modes in the system, we require the state to reproduce itself after one round trip:

$$\psi_\mathrm{IV} = e^{i\Theta}\psi_\mathrm{I} \tag{S4}$$

This requires finding the eigenvalues of the roundtrip transfer matrix T, which is the product of the previous three transfer matrices:

$$\psi_\mathrm{IV} = T\psi_\mathrm{I}, \quad T = e^{in_\mathrm{wg}\omega\overline{L}/c}\begin{pmatrix}e^{-in_\mathrm{wg}\omega\Delta L/c}\cos(g_\mathrm{co}L_\mathrm{co}) & i\sin(g_\mathrm{co}L_\mathrm{co})\\ i\sin(g_\mathrm{co}L_\mathrm{co}) & e^{in_\mathrm{wg}\omega\Delta L/c}\cos(g_\mathrm{co}L_\mathrm{co})\end{pmatrix} \tag{S5}$$

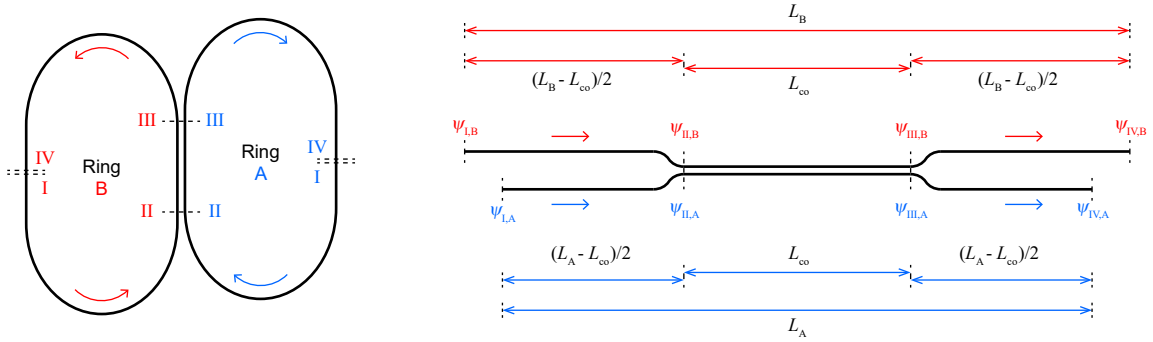

FIG. S1. Schematic of the two-ring coupled resonator. Left panel: Top view of the coupled resonator with key points marked. Right panel: Schematic of the resonator with straightened waveguides (not to scale). Segment lengths and field amplitudes have been marked.

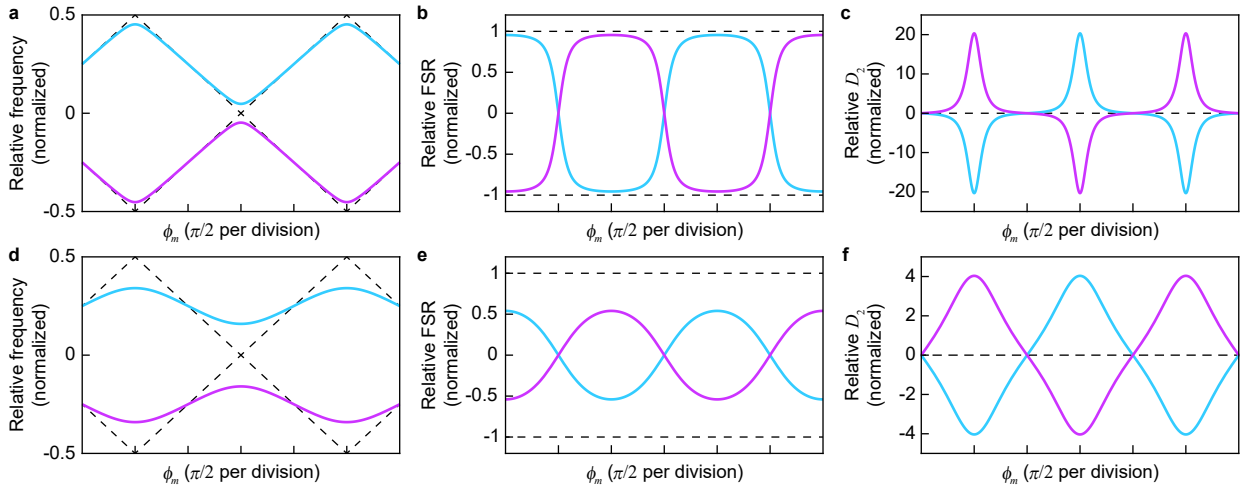

FIG. S2. Eigenfrequency plots for the two-ring coupled resonator. **a-c** Relative frequency (normalized to $D_{1,m}$), relative FSR (normalized to $\epsilon D_{1,m}$) and relative D_2 (normalized to $\epsilon^2 D_{1,m}$) plots for $g_{\rm co}L_{\rm co} = 0.3$. **d-f** Similar plots but with $g_{\rm co}L_{\rm co} = 1.0$. The horizontal axis is defined as $\phi_m = 2\pi\epsilon m$. Relative mode frequency, FSR and D_2 for individual rings before coupling have been superimposed (black dashed lines). The relative FSR is found by differentiating the relative frequency, and the relative D_2 is found by differentiating the relative FSR.

where $\overline{L} = (L_{\rm A} + L_{\rm B})/2$ and $\Delta L = (L_{\rm B} - L_{\rm A})/2$. Each one of the two eigenvalues defines a transverse mode family of the system. Furthermore, when the accumulated phase Θ equals an integer multiple of 2π, a longitudinal mode can be found at the corresponding frequency. Diagonalizing the T matrix gives

$$\Theta = n_{\rm wg}\omega\overline{L}/c \mp \arccos[\cos(g_{\rm co}L_{\rm co})\cos(n_{\rm wg}\omega\Delta L/c)] \tag{S6}$$

Now we define a mode number associated with the average length of the rings:

$$m \equiv \frac{n_{\rm wg}\omega\overline{L}}{2\pi c} \tag{S7}$$

The relation can be inverted to give a solution of ω_m dependent on m. When m is an integer, ω_m would be the mode frequencies for a ring resonator with length $\overline{L}$. As $g_{\rm co} \ll \omega/c$ and $\Delta L \ll \overline{L}$, the phase contribution related to the coupling varies slowly compared to the $n_{\rm wg}\omega\overline{L}/c$ part. This allows us to approximate the coupled mode frequencies using ω_m, and the eigenfrequencies $\omega_{m,\pm}$ can be solved as:

$$\begin{aligned} 2\pi m &= n_{\rm wg}\omega_{m,\pm}\overline{L}/c \mp \arccos[\cos(g_{\rm co}L_{\rm co})\cos(n_{\rm wg}\omega_{m,\pm}\Delta L/c)] \\ &\approx n_{\rm wg}\omega_{m,\pm}\overline{L}/c \mp \arccos[\cos(g_{\rm co}L_{\rm co})\cos(n_{\rm wg}\omega_m\Delta L/c)] \end{aligned} \tag{S8}$$

$$\begin{aligned} \omega_{m,\pm} &= \omega_m \pm \left[\frac{\overline{L}}{c}\frac{\partial(n_{\rm wg}\omega)}{\partial\omega}\right]^{-1}\Bigg|_{\omega=\omega_m} \times \arccos\left[\cos(g_{\rm co}L_{\rm co})\cos\left(2\pi\frac{\Delta L}{\overline{L}}m\right)\right] \\ &= \omega_m \pm \frac{D_{1,m}}{2\pi}\arccos\left[\cos(g_{\rm co}L_{\rm co})\cos\left(2\pi\epsilon m\right)\right] \end{aligned} \tag{S9}$$

where $D_{1.m}$ is the local FSR that depends on ω_m and $\epsilon = \Delta L/\overline{L}$ is the length contrast of the rings. The result shows that the mode structure can be seen as splitting off from the length-averaged resonator modes, where the splitting gap is determined by $g_{\rm co}$ and modulated with respect to mode number with period ϵ^{-1}. Note that Eq. (2) in the main text is obtained by replacing the mode number m with the relative mode number μ in Eq. (S9). Such a variable change is valid when μ is referenced to a frequency degeneracy of the rings.

To gain insight into the model, Fig. S2 plots mode frequency, FSR and the second-order dispersion parameter D_2 relative to ω_m for different values of $g_{\rm co}$ as predicted by Eq. (S9). In these plots ω_m has been subtracted from the mode frequencies, and only the contributions associated with FSR difference of the two rings and the coupling are considered. The $D_{1,m}$ is also approximated as a constant. The FSRs of the transverse modes show a typical avoided crossing behavior as shown in Fig. S2b and S2e. The FSR of one mode continuously transitions to the other mode

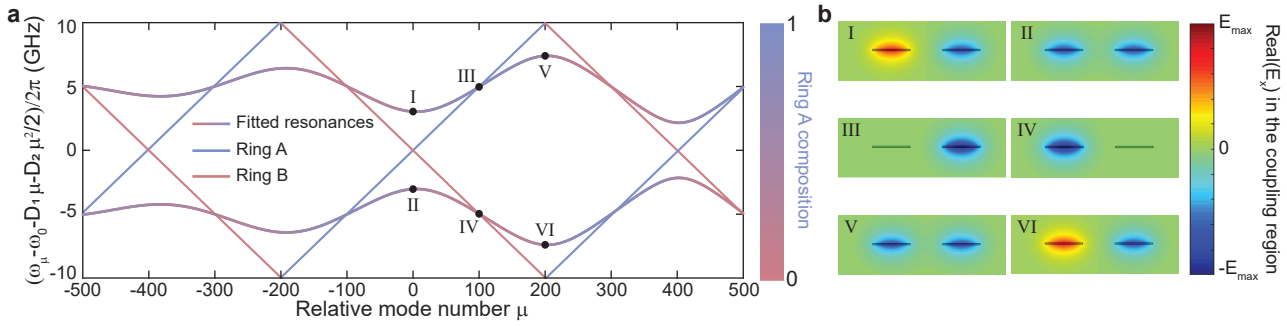

FIG. S3. Illustration of mode hybridization in the coupling region. This figure reproduces Extended Data Fig. 2a and 2b from the main text. **a** Fitted optical resonance frequency dispersion of the coupled resonator (solid curves) and fitted mode frequency dispersion of the single rings (red and blue lines) plotted versus relative mode number μ. These plots are the same as Fig. 2c in the main text. **b** Cross-sectional view of simulated electric field amplitudes in the coupled region at mode numbers indicated in panel **a** by the black points. The right (left) waveguide belongs to ring A (B). At the crossing center (I, II, V and VI), two waveguides have the same field intensity and the opposite (same) phase for the anti-symmetric (symmetric) mode. When hybrid mode frequencies meet the single-ring resonances (III and IV), the electrical field at the coupled region is contributed by a single ring.

at the avoided crossing, and similar to the coupling itself, this process is also periodic in the frequency domain. The calculated D_2 shows spikes at the avoided crossing center, and the positive spike can be used to counter the normal dispersion present in the averaged resonator dispersion. Smaller $g_{\rm co}$ leads to higher peak D_2 with smaller crossing bandwidth. To get a larger crossing bandwidth, $g_{\rm co}$ could be increased at the expense of lower D_2, but the maximum bandwidth is half the modulation period (i.e. the Vernier FSR) as the effect of the neighboring crossings set in and shifts the D_2 in the opposite direction.

In addition to the mode frequency, the mode compositions can also be derived from the transfer matrix T. As the change of mode profile is large enough across the measured optical bandwidth, the mode compositions has an impact on soliton power distribution in the rings (as in Fig. 1b in the main text), and complements FSRs and dispersions when describing the dispersion characteristics. The eigenvectors of T read,

$$\psi_{\rm I} \propto \left(\sqrt{\frac{\sin(\alpha \pm \phi_m)}{2\sin\alpha\cos\phi_m}},\ \mp\sqrt{\frac{\sin(\alpha \mp \phi_m)}{2\sin\alpha\cos\phi_m}} \right)^{\mathbf{T}},\quad \phi_m = 2\pi\epsilon m,\quad \alpha = \arccos\left[\cos(g_{\rm co}L_{\rm co})\cos\phi_m\right] \tag{S10}$$

This gives the relative field intensities in the non-coupled regions of the rings for a particular mode. Another point of interest is the center of the coupled region. Here the field can be found as

$$\psi_{\rm co} \propto \begin{pmatrix} \cos(g_{\rm co}L_{\rm co}/2) & i\sin(g_{\rm co}L_{\rm co}/2) \\ i\sin(g_{\rm co}L_{\rm co}/2) & \cos(g_{\rm co}L_{\rm co}/2) \end{pmatrix} \begin{pmatrix} e^{-i\phi_m/2} & 0 \\ 0 & e^{i\phi_m/2} \end{pmatrix} \psi_{\rm I} \propto \left(\sqrt{\frac{\sin\alpha \pm \sin\phi_m}{2\sin\alpha}},\ \mp\sqrt{\frac{\sin\alpha \mp \sin\phi_m}{2\sin\alpha}} \right)^{\mathbf{T}} \tag{S11}$$

Similarly, the optical field at any point z in the rings can be calculated and is denoted as $\psi_{\rm A(B)}(z)$. The fractional energy contribution from ring A ($\eta_{\rm A}$) reads as

$$\eta_{\rm A} = \frac{\int_{\rm A} |\psi_{\rm A}(z)|^2 dz}{\int_{\rm A} |\psi_{\rm A}(z)|^2 dz + \int_{\rm B} |\psi_{\rm B}(z)|^2 dz} \tag{S12}$$

which is used to color Fig. 2b and Fig. 2c in the main text.

There are some special cases of ϕ_m that lead to simplified field distributions and are demonstrated in Fig. S3. For example, if ϕ_m/π is an integer (crossing centers), the modes become purely symmetrical and anti-symmetrical:

$$\psi_{\rm I} \propto (\sqrt{1/2}, \mp\sqrt{1/2})^{\mathbf{T}},\quad \psi_{\rm co} \propto (\sqrt{1/2}, \mp\sqrt{1/2})^{\mathbf{T}}, \tag{S13}$$

Points I, II, V, and VI in Fig. S3b belong to these cases. Points II and V are symmetric modes formed by the two rings, with equal mode intensities and the same phase. On the other hand, points I and VI are anti-symmetric modes, with equal mode intensities but opposite phase. These results happen to agree with coupled-mode calculations when only the pair of degenerate longitudinal modes from each ring are considered. However, while the energy is equally distributed in the two rings in the same way as the reduced coupled-mode theory predicted, other longitudinal modes

still participate in the coupling because the wavevector in the coupled region differs from that in the uncoupled region. On the other hand, if ϕ_m/π is a half-integer (halfway between crossing centers), then at the center of coupling position the field is entirely within a single ring:

$$\psi_{\mathrm{I}} \propto (\cos(g_{\mathrm{co}}L_{\mathrm{co}}/2), \mp\sin(g_{\mathrm{co}}L_{\mathrm{co}}/2))^{\mathbf{T}}, \quad \psi_{\mathrm{co}} \propto (1,0)^{\mathbf{T}}, \quad \text{or} \quad \psi_{\mathrm{I}} \propto (\sin(g_{\mathrm{co}}L_{\mathrm{co}}/2), \pm\cos(g_{\mathrm{co}}L_{\mathrm{co}}/2))^{\mathbf{T}}, \quad \psi_{\mathrm{co}} \propto (0,-1)^{\mathbf{T}}, \tag{S14}$$

Points III and IV in Fig. S3b belong to these cases.

An interesting feature of the field distribution is that, for a single continuous branch, the field compositions exchange parity at the next degeneracy point, and the anti-symmetric mode now becomes the symmetric mode (from point I to V) and vice versa (from point II to VI). The change of parity shows that the modes repeat themselves every two Vernier periods (every two degeneracy points) instead of one, in agreement with Eq. (S9). While the parity exchange is obvious after plotting the dispersion (Fig. S3a), it can also be understood from a mode number argument. We consider the total phase accumulated in ring A for a specific mode divided by 2π, which should be an integer and denoted as m_{A}. This is the "mode number" for ring A for the specific mode. Similarly m_{B} could be defined. These two numbers equal to the respective mode numbers of the closest uncoupled modes, which can be seen by adiabatically turning off the coupling. For a single Vernier period, the total mode number changes by an odd number. However, going to the next longitudinal mode by changing the frequency alone changes both m_{A} and m_{B} by one. The only way to induce a separate mode number change is to create a zero in the field amplitude somewhere in the respective ring, which is indeed the case for points III and IV shown in Fig. S3b. Considering that the individual mode numbers are about equally distributed around the averaged-length mode number m (e.g. $|(m_{\mathrm{B}}-m)-(m-m_{\mathrm{A}})| \leq 1$), the extra increment of m_{B} and decrement of m_{A} should have taken place alternatively between the Vernier periods, indicating the mode branch switches mode compositions for each Vernier period.

II. EIGENMODES OF A THREE-RING COUPLED RESONATOR

In this section we study the mode frequencies of the three-ring coupled resonator. Although the derivation is similar to that of the two-ring resonator, we will highlight some features of the coupled system that are not obvious in the two-ring case. The result can also be readily generalized to multi-ring arrangements.

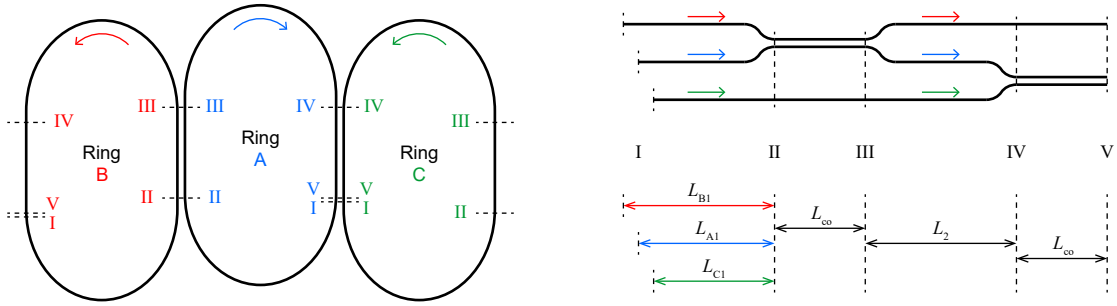

FIG. S4. Schematic of the three-ring coupled resonator. Left panel: Top view of the coupled resonator with key points marked. Right panel: Schematic of the resonator with straightened waveguides (not to scale). Segment lengths have been marked.

The schematic for the three-ring coupled resonator is shown in Fig. S4 along with definitions of segment lengths. Unlike the two-ring case, there is no explicit symmetry to take advantage of, and the segmentation method is chosen to reduce calculation complexity. We can assemble the field amplitudes from ring C, A and B, in that order, into a vector and find the transfer matrix for each section:

$$\psi_{\mathrm{II}} = \exp\left[in_{\mathrm{wg}}\omega/c \begin{pmatrix} L_{\mathrm{C1}} & 0 & 0 \\ 0 & L_{\mathrm{A1}} & 0 \\ 0 & 0 & L_{\mathrm{B1}} \end{pmatrix}\right]\psi_{\mathrm{I}} \tag{S15}$$

$$\psi_{\mathrm{III}} = \exp\left[iL_{\mathrm{co}} \begin{pmatrix} n_{\mathrm{wg}}\omega/c & 0 & 0 \\ 0 & n_{\mathrm{wg}}\omega/c & g_{\mathrm{co}} \\ 0 & g_{\mathrm{co}} & n_{\mathrm{wg}}\omega/c \end{pmatrix}\right]\psi_{\mathrm{II}} \tag{S16}$$

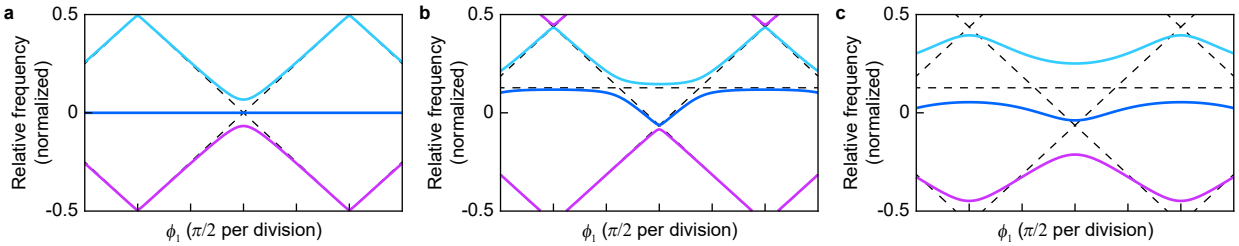

FIG. S5. Eigenfrequency plots for the three-ring coupled resonator, showing relative frequency (normalized to $D_{1,m}$) versus ϕ_1. Parameters are **a** $g_{\rm co}L_{\rm co} = 0.3$ and $\phi_2 = 0$; **b** $g_{\rm co}L_{\rm co} = 0.3$ and $\phi_2 = 0.4$; **c** $g_{\rm co}L_{\rm co} = 1.0$ and $\phi_2 = 0.4$.

$$\psi_{\rm IV} = \exp\left[in_{\rm wg}\omega/c\begin{pmatrix} L_2 & 0 & 0 \\ 0 & L_2 & 0 \\ 0 & 0 & L_2 \end{pmatrix}\right]\psi_{\rm III} \tag{S17}$$

$$\psi_{\rm V} = \exp\left[iL_{\rm co}\begin{pmatrix} n_{\rm wg}\omega/c & g_{\rm co} & 0 \\ g_{\rm co} & n_{\rm wg}\omega/c & 0 \\ 0 & 0 & n_{\rm wg}\omega/c \end{pmatrix}\right]\psi_{\rm IV} \tag{S18}$$

The overall round-trip transfer matrix is the product of the previous four matrices and reads

$$T = \begin{pmatrix} e^{in_{\rm wg}\omega L_{\rm C}/c}\cos(g_{\rm co}L_{\rm co}) & ie^{in_{\rm wg}\omega L_{\rm A}/c}\cos(g_{\rm co}L_{\rm co})\sin(g_{\rm co}L_{\rm co}) & -e^{in_{\rm wg}\omega L_{\rm B}/c}\sin^2(g_{\rm co}L_{\rm co}) \\ ie^{in_{\rm wg}\omega L_{\rm C}/c}\sin(g_{\rm co}L_{\rm co}) & e^{in_{\rm wg}\omega L_{\rm A}/c}\cos^2(g_{\rm co}L_{\rm co}) & ie^{in_{\rm wg}\omega L_{\rm B}/c}\cos(g_{\rm co}L_{\rm co})\sin(g_{\rm co}L_{\rm co}) \\ 0 & ie^{in_{\rm wg}\omega L_{\rm A}/c}\sin(g_{\rm co}L_{\rm co}) & e^{in_{\rm wg}\omega L_{\rm B}/c}\cos(g_{\rm co}L_{\rm co}) \end{pmatrix} \tag{S19}$$

where we defined the total length of ring C, $L_{\rm C} = L_{\rm C1} + L_2 + 2L_{\rm co}$, and $L_{\rm A}$ and $L_{\rm B}$ are defined similarly. Note that the dependence on individual segment lengths $L_{\rm C1}$, $L_{\rm A1}$, $L_{\rm B1}$ and L_2 have disappeared from T, indicating that the relative position of the couplers on ring A does not matter for eigenfrequency calculations. This is because propagating the same distance for all three components provides only a global phase for the state, which can be moved past the coupler. Mathematically, the coupling matrix commutes with the propagation matrix, which is proportional to the identity matrix for identical ring cross sections:

$$\left[L_{\rm co}\begin{pmatrix} n_{\rm wg}\omega/c & 0 & 0 \\ 0 & n_{\rm wg}\omega/c & g_{\rm co} \\ 0 & g_{\rm co} & n_{\rm wg}\omega/c \end{pmatrix},\ n_{\rm wg}\omega/c\begin{pmatrix} L_2 & 0 & 0 \\ 0 & L_2 & 0 \\ 0 & 0 & L_2 \end{pmatrix}\right] = 0 \tag{S20}$$

For the coupler itself, the propagating part (diagonal elements) also commute with the pure coupling part (off-diagonal elements), although different couplers do not commute. Therefore, the system is equivalent to propagating along the entire length of individual rings, followed by two point couplers with the same coupling ratios as the original couplers. This argument works for all coupled resonators with identical ring cross-sections coupled in a chain or tree topology, and provides a degree of freedom for placing the rings in the design phase.

Following the two-ring analysis, we define an averaged length for the resonators and its associated mode number:

$$\overline{L} \equiv \frac{L_{\rm C} + L_{\rm A} + L_{\rm B}}{3},\quad m \equiv \frac{n_{\rm wg}\omega\overline{L}}{2\pi c} \tag{S21}$$

We will also need to define two length differences. For the current design, we have $L_{\rm C} + L_{\rm B} \approx 2L_{\rm A}$, and the following contrast definitions become convenient:

$$\epsilon_1 = \frac{L_{\rm B} - L_{\rm C}}{2\overline{L}},\quad \epsilon_2 = \frac{L_{\rm C} + L_{\rm B} - 2L_{\rm A}}{6\overline{L}} \tag{S22}$$

With these notations, T can be written as

$$T = e^{2\pi mi}\begin{pmatrix} e^{i(-\phi_1+\phi_2)}\cos(g_{\rm co}L_{\rm co}) & ie^{-2i\phi_2}\cos(g_{\rm co}L_{\rm co})\sin(g_{\rm co}L_{\rm co}) & -e^{i(\phi_1+\phi_2)}\sin^2(g_{\rm co}L_{\rm co}) \\ ie^{i(-\phi_1+\phi_2)}\sin(g_{\rm co}L_{\rm co}) & e^{-2i\phi_2}\cos^2(g_{\rm co}L_{\rm co}) & ie^{i(\phi_1+\phi_2)}\cos(g_{\rm co}L_{\rm co})\sin(g_{\rm co}L_{\rm co}) \\ 0 & ie^{-2i\phi_2}\sin(g_{\rm co}L_{\rm co}) & e^{i(\phi_1+\phi_2)}\cos(g_{\rm co}L_{\rm co}) \end{pmatrix} \tag{S23}$$

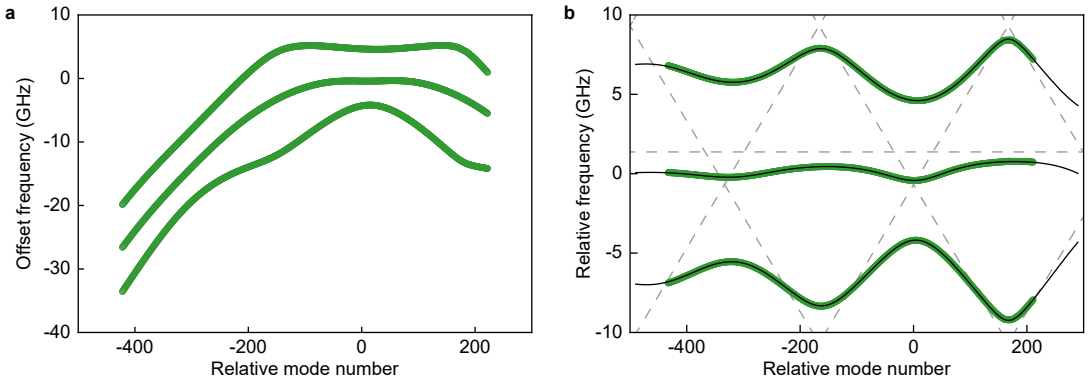

FIG. S6. Dispersion of the three-ring resonator. **a** Measured dispersion for the three-ring resonator. The topmost branch is also shown in Fig. 1e in the main text. **b** Mode frequencies relative to the averaged frequencies (circles). Solid curves show the fitted result using the three-ring model, and are in excellent agreement with the data. Dashed lines indicate frequencies of the individual rings before coupling.

with $\phi_1 = 2\pi\epsilon_1 m$ and $\phi_2 = 2\pi\epsilon_2 m$. For the current design, $\epsilon_1 \approx 3 \times 10^{-3}$ and $\epsilon_2 \approx 1.5 \times 10^{-6}$, which ensures a slowly-varying phase contributed by the coupling. The eigenfrequencies are given by

$$\omega = \omega_m - \frac{D_{1,m}}{2\pi}\theta \tag{S24}$$

where $e^{i\theta}$ is given by the roots to the cubic characteristic equation:

$$x^3 - (e^{-2i\phi_2}\cos(g_{\rm co}L_{\rm co}) + 2e^{i\phi_2}\cos(\phi_1))\cos(g_{\rm co}L_{\rm co})x^2 + (e^{2i\phi_2}\cos(g_{\rm co}L_{\rm co}) + 2e^{-i\phi_2}\cos(\phi_1))\cos(g_{\rm co}L_{\rm co})x - 1 = 0, \quad x \equiv e^{i\theta} \tag{S25}$$

The unitary nature of T ensures that all three roots for x lie on the complex unit circle.

As $\epsilon_2 \ll \epsilon_1$ for the current design, ϕ_2 varies much more slowly compared to ϕ_1 and we will take ϕ_2 to be a constant to simplify the discussions below. Fig. S5 plots the relative frequencies for some parameter combinations. In the case of $\phi_2 = 0$ (Fig. S5a), the mode frequencies of ring A coincides with the averaged frequency, and the mode frequencies of ring A and B are symmetrically distributed around the averaged frequency. As a result, the coupled frequency spectrum resembles that of the two-ring resonator. A key difference here is that the two gaps opened have different widths. For crossings at integer $\phi_1/(2\pi)$ locations, ring A participates in the coupling, and the total gap is approximately $2\sqrt{2}g_{\rm co}L_{\rm co} \times D_{1,m}/(2\pi)$ for small $g_{\rm co}L_{\rm co}$. For the other crossings at half-integer $\phi_1/(2\pi)$ locations, the mode from ring A is half an FSR away from ring C and B, and the coupling becomes indirect. Here the gap width is approximately $(g_{\rm co}L_{\rm co})^2 \times D_{1,m}/(2\pi)$ for small $g_{\rm co}L_{\rm co}$, which is second order in the coupling strength. A nonzero $\phi_2 = 0$ breaks the frequency-domain symmetry and leads to additional avoided crossings (Fig. S5b). For stronger coupling strengths, the bandwidths of the crossings expand and merge with the other crossings (Fig. S5c) similar to the two-ring case. Here the frequency dispersion become smoother and have less overall coupling-contributed dispersion.

Figure S6a shows the measured dispersion data for the three-ring resonator. The topmost branch is used for soliton generation and is also shown in Fig. 1e in the main text. Fitting the averaged frequency (not plotted) gives an averaged FSR of 19.9711 GHz and a second-order dispersion parameter of 282.7 kHz, consistent with the two-ring results. After subtracting the averaged frequency, Fig. S6b shows the relative frequency with a similar structure of Fig. S5c. Using the exponential decaying coupling model as described in the methods ($g_{\rm co} = g_{\rm co,0}\exp(-\mu/\mu_g)$), the fitted result for the relative frequencies also shows good agreement with the measured data. The fitted parameters are $g_{\rm co,0}L_{\rm co} = 0.985$, $\mu_g = 1175$ and $\phi_2 = 0.216$.